Tectonophysics 819 (2021) 229069

Contents lists available at ScienceDirect

Tectonophysics

journal homepage: www.elsevier.com/locate/tecto

Asymmetry of faults and stress patterns within the Dead Sea basin as displayed by seismological analysis

Nadav Wetzler [a,*], Amir Sagy [a], Shmuel Marco [b], Ze'ev Reches [c]

[a] The Geological Survey of Israel, Jerusalem, Israel
[b] The Department of Geophysics, Tel Aviv University, Tel Aviv, Israel
[c] School of Geosciences, University of Oklahoma, Norman, OK, USA

ARTICLE INFO

Keywords:
Stress-inversion
Pull-apart basins
Frictional strength
Earthquakes
Focal-mechanism
Dead Sea transform
b-value

ABSTRACT

The Dead Sea pull-apart basin (DSB), which is located within the Dead Sea Transform fault system, displays tectonic asymmetry between its eastern and western longitudinal zones. We investigate the seismological and mechanical signature of this asymmetry by the analyzing the hypocenter distribution and focal-mechanisms of 114 Mw = 1.5–5.2 earthquakes recorded from 1985 till 2012. The analysis indicates that the seismicity along the western longitudinal zone is deeper than the eastern one. Focal mechanism analysis indicates that about 50% of solutions are strike-slip, compatible with the plate motions along the Dead Sea transform. Comparison between the two longitudinal zones of the basin shows that the focal mechanisms in the eastern DSB are dominated by strike-slip faulting shallower than 12 km depth, whereas those in the western DSB are dominated by oblique faulting below 12 km depth. The *b* value of the Gutenberg-Richter magnitude distributions also show difference between the two zones with ~0.9 in the west and ~0.7 in the east zone.

We develop stress-inversion analysis to identify the fault planes of the focal mechanisms by using friction-dependent selection process. The horizontal maximum compression (σ_{Hmax}) trends NNW-SSE, with increasing value of the vertical stress component along the western part of the basin, corresponds to the oblique faulting in this zone. The optimal friction coefficient determined by the stress-inversion for the fault planes is $\mu \sim 0.5$. Our analysis emphasizes the significant contribution of frictional dependent stress-inversion as an effective tool in seismotectonic analysis.

1. Introduction

Pull-apart basins along transform plate boundaries are considered as depressional regions between two sub-parallel segments of strike-slip faults (Aydin and Nur, 1982; Freund, 1974; Reches, 1987; Sylvester, 1988). While these basins may be idealized as a rhomb-shaped basin formed by two longitudinal faults and terminated by two transverse faults, geophysical surveys reveal complex, internal 3D structures (e.g. Brothers et al., 2009; Imren et al., 2001; Lubberts and Ben-Avraham, 2002; ten-Brink et al., 1989). These structures indicate that the large-scale plate motions are accommodated by distributed slip along multiple intra-basin secondary faults (e.g. Ben-Avraham and ten-Brink, 1989).

The hypocenters inside the basin can highlight the subsurface fault patterns at depth (Braeuer et al., 2012; Wetzler et al., 2014), beyond the resolution of deep refraction surveys (Ginzburg and Ben-Avraham, 1997; Mechie et al., 2009). Focal-mechanism solutions are commonly used to determine faulting geometry and stress field patterns (e.g. Palano et al., 2013). Due to the scarcity of large earthquakes, seismotectonic analyses of regions of low-to-moderate seismicity rate frequently rely on micro-earthquakes (Brodsky, 2019). However, due to the symmetry of the radiation pattern of double couple sources, additional independent information of the fault geometry is required to identify the fault planes of the focal mechanisms. Stress-inversion methods had been used to distinguish between the fault and the auxiliary planes (Rivera and Cisternas, 1990). Incorporation of friction coefficient in the stress-inversion can delineate the regional stress field together with selecting the fault planes using realistic mechanical conditions (Vavryčuk, 2014).

The friction coefficient might vary with the applied normal stress (e.g., Lockner, 1998), and can reflect spatial rheological heterogeneity in the crust (Provost and Houston, 2003). The conditions of shear along surface are generalized by the Coulomb-Mohr criterion $|\tau| = \mu\sigma_n$, where

* Corresponding author.
E-mail address: nadavw@gsi.gov.il (N. Wetzler).

https://doi.org/10.1016/j.tecto.2021.229069
Received 18 January 2021; Received in revised form 26 August 2021; Accepted 9 September 2021
Available online 22 September 2021
0040-1951/

τ and σ_n are the magnitudes of the shear (in the slip direction) and normal stresses, and μ is the coefficient of friction.

We explore the fault kinematics and the regional stress field of the Dead Sea basin (DSB). The DSB is a pull-apart system located at an active plate boundary, the Dead Sea transform fault system, as manifested by the intra-basinal small earthquakes (Fig. 1a). The Dead Sea transform fault system has been active since the Miocene, and accumulated ~100 km of sinistral displacement with an average geologic slip rate of 5 mm/yr (Garkunkel, 1981), consistent with the ~4–5 mm/y GPS measurements (Palano et al., 2013). The crust of the DSB includes a ~ 10 km thick sedimentary sequence that manifests the subsidence of the basin (ten-Brink and Flores, 2012). The internal structure of the DSB was recognized as an asymmetric basin formation with localized deformation of the on the east side and more diffuse deformation in the west (Ben-Avraham, 1992; Ben-Avraham and Zoback, 1992; Zak and Freund, 1981). Further geological (Garfunkel and Ben-Avraham, 1996), geophysical (Al-Zoubi et al., 2002), and seismological studies (Braeuer et al., 2014; Braeuer and Bauer, 2015; Shamir, 2007) support the general

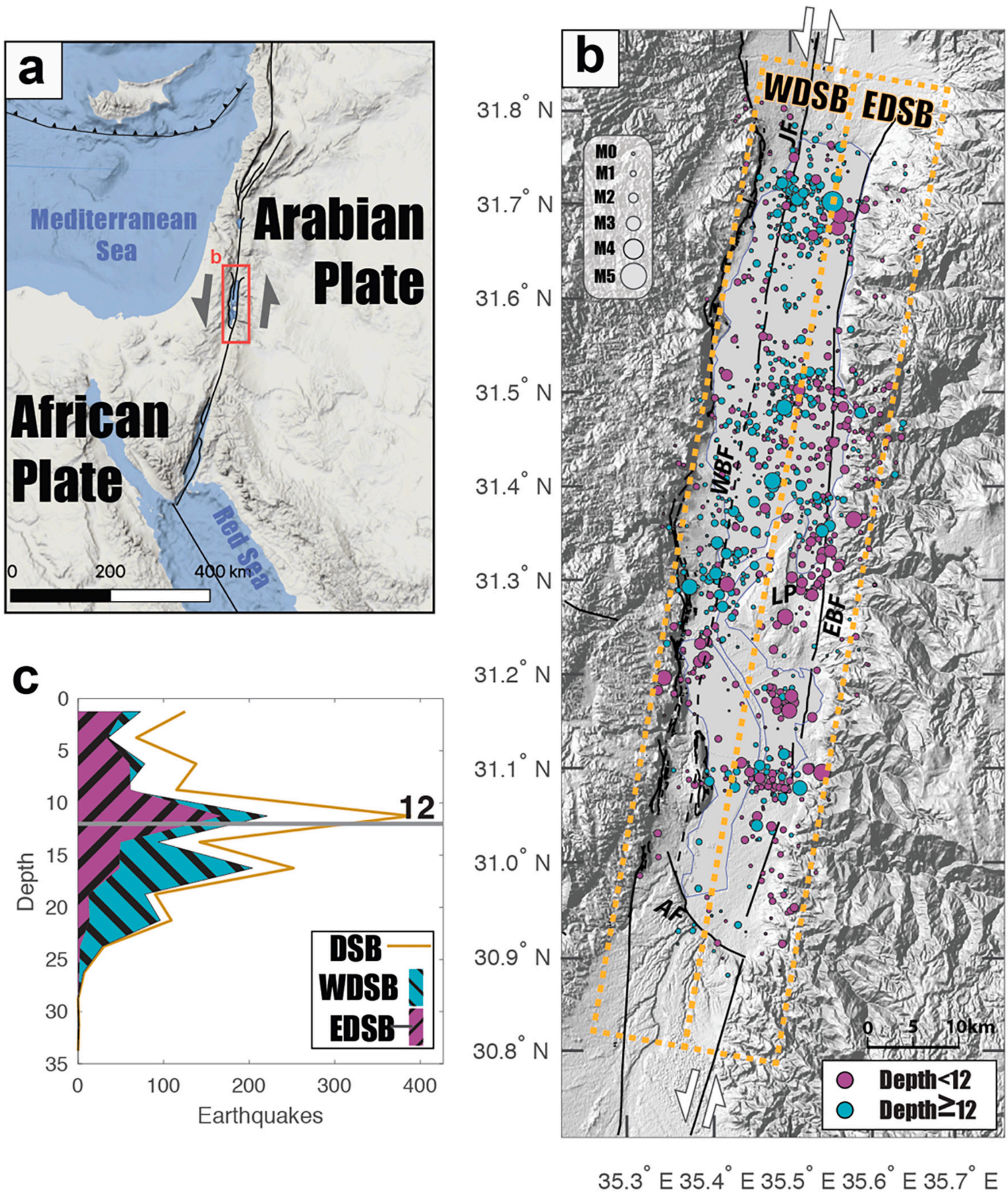

Fig. 1. (a) General tectonic map of Dead Sea transform system (black solid lines), including study area (red rectangle). (b) Seismicity at the Dead Sea basin for the 1985–2021 period. Events are colour-coded for two focal depth (above and below 12 km depth), and magnitude size shown in legend. Event locations by the Israel National Seismic Network (https://earthquake.co.il). Also plotted: main fault (black lines) (after Sharon et al., 2020), Lisan Peninsula salt diapir (*LP*); Eastern Boundary fault (*EBF*); Western Boundary fault (*WBF*); and Jericho fault (*JF*). The dashed-orange rectangles divide the Dead Sea basin into the Eastern DSB (EDSB) zone and the Western DSB (WDSB) zone. (c) Depth distribution of the seismic events shown for the WDSB and EDSB zones, and basin wide (DSB); grey horizontal line at 12 km depth divides to upper and lower groups. We note a clear spatial difference in the focal depth. (For interpretation of the references to colour in this figure legend, the reader is referred to the web version of this article.)

asymmetric faulting structure of the DSB. However, it is still unclear how does the plate motions are expressed by the deformation and earthquake activity inside the basin, and how seismicity reflects the plates motion and stress.

The largest instrumentally-recorded event in the DSB is the M 6.21927 North Dead Sea earthquake (Shapira et al., 1993; Zohar and Marco, 2012), with about 500 casualties. Paleoseismic records (Agnon, 2014) and historical records (Zohar et al., 2017) suggest that earthquakes along the Dead Sea fault system can reach Mw 7.5. The largest earthquake in the DSB during the analyzed period was the Mw 5.2 11 February 2004, strike-slip event, located at the northern part of the basin (event #2337, Fig. 2a). This earthquake has a N-S preferred nodal fault plane (Hofstetter et al., 2008), associated with the continuation of the Jericho Fault (Wetzler et al., 2014, see Fig. 1b for the location of the Jericho Fault). Wetzler et al. (2014) recognized earthquakes clusters within the DSB, and attributed the larger magnitude earthquakes with the longitudinal faults. The seismicity at the central part of the basin reveals a “v” shaped basin with a steeply dipping fault zone at the eastern border of the basin and a belt of normal faults and eastward tilting blocks along the western boundary (Sagy et al., 2003) with a moderately eastward dipping seismicity (Braeuer et al., 2014; Braeuer and Bauer, 2015). Focal mechanism solutions indicate a dominant strike-slip faulting, mostly associated with the longitudinal faults and minor right-lateral movement along east-west-fault strikes at the southern part of the basin (Hofstetter et al., 2007, 2016). Hofstetter et al. (2007) and Palano et al. (2013) calculated stress field based on 27 focal mechanisms (1987–1995). A stress-inversion analysis of DSB earthquakes by Hofstetter et al. (2016) included smaller magnitude earthquakes, down to $M_d - 0.5$, within a relatively small part of the basin for a period of 18 months. Nine sub-regions were defined, and stress states were calculated based on the focal mechanisms population in each sub-region. Four clusters along the eastern longitudinal fault fit the paleo-stress field determined by Eyal and Reches (1983) in the Israel-Sinai subplate based on meso-structures outcrops with σ_{Hmax} and σ_{hmin} trending of NNW and WSW, respectively.

We analyze the tectonic significant of small earthquakes during a 35 year period in a region of low-to-intermediate seismicity rate. We first analyze the spatial and temporal distribution of the events, and then

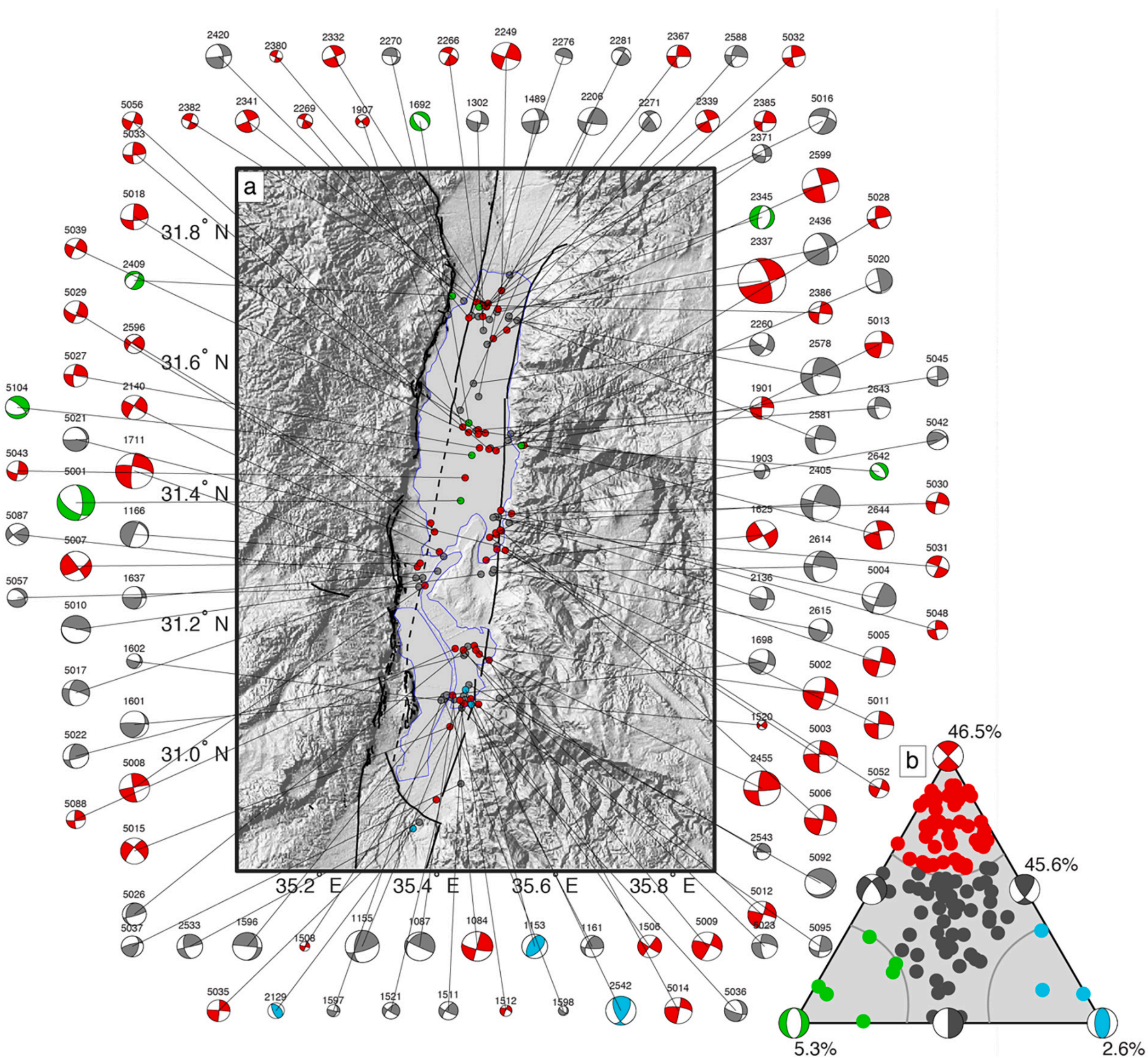

Fig. 2. (a) Focal mechanism solutions of earthquakes from the Dead Sea basin for the 1985–2021 period with earthquake magnitudes of $M_W = 1.5$–5.2. Shown 114 solutions of strike-slip (red), normal (green), reverse (light blue), and oblique (grey) faulting; also plotted are the main fault (black lines) and the 2021 lake coastline (blue lines). (b) Ternary plot of faulting styles based on the plunge angles of the P, T and B axes of the focal mechanism solutions (after Frohlich, 2001); frequency percentage of end members are displayed at each node. Most of the focal mechanism solutions show strike-slip and oblique faulting. (For interpretation of the references to colour in this figure legend, the reader is referred to the web version of this article.)

calculate 114 focal mechanisms to characterize the faulting style. Finally, we apply stress-inversion analysis to calculate the intra-basin stress field, while exploring the stress field over a wide range of frictional levels and testing the compliance of our datasets to a few possible internal stress fields. The stress inversion discriminates between the fault plane and auxiliary focal mechanisms nodal plane and estimate the optimal friction coefficient within the DSB.

2. Dataset and analytical methods

2.1. Dead Sea seismicity

Earthquakes in the DSB region are recorded by the regional network (Fig. S1) and are systematically manually analyzed since the 1980's (https://earthquake.co.il). The seismic distribution in the DSB generally shows a depth dependent spatial distribution (Fig. 1b). The spatial trend of the depth distribution indicates that the seismicity along the western boundary of the basin (WDSB, Fig. 1b) is deeper than along the eastern part of the basin (EDSB, Fig. 1b). We consider this depth difference as a primary indication for asymmetry comparing the two sides of the DSB (Figs. 1c, S2).

Additional evidence for the asymmetric seismicity comes from the earthquake magnitudes distribution. Strike-slip regions show Gutenberg-Richter b values of 0.9–1.0, (Schorlemmer et al., 2005). Magnitude of completeness (Mc) and b value for seismicity inside the DSB between 01-Jan-1985 and 18-Apr-2021 is computed iteratively from the goodness of fit between observed and theoretical Gutenberg–Richter distributions using a Kolmogorov-Smirnov test with b value from maximum likelihood estimation. We select Mc for the minimum difference between the distributions is negligible. More specifically, we use the minimum as the definition of goodness of fit from the Kolmogorov-Smirnov metric distance between the two cumulative distribution functions. The determined Gutenberg–Richter distributions with estimated Mc indicate the $b \approx 0.9$ for WDSB (Fig. 3a) relatively low $b \approx 0.7$ for EDSB (Fig. 3b).

2.2. Dead Sea focal-mechanism

We compute here focal mechanisms between 1985 and 2021. For earthquakes between 1985 and 2010 we use the relocated catalog of Wetzler et al. (2014), which includes ~1100 earthquakes of Mw =1.5–5.2 (Fig. 2a). For this dataset, focal mechanisms are calculated using the USGS HASH program (Hardebeck and Shearer, 2002), which provides the most likely mechanism from the P-wave first-motion polarities using the regional seismic velocity model of Gitterman et al. (2002). P-wave first motions were manually picked, and focal mechanisms were only calculated for earthquakes located within the DSB, with at least 10 unambiguous polarities to ensure reliable solutions resulting 66 earthquakes.

For the 2010–2021 period, we use the original locations of the Israel Seismic Network catalog, relaying on improved locations since 2010 due to the addition of ~100 seismic stations (Nof and Kurzon, 2020) with an average location errors of 0.223 km at south-north, and 0.105 km at the east-west directions. For this time period we compute focal mechanisms using the full-waveform time-domain moment tensor (TDMT) technique (Dreger and Helmberger, 1993), which implemented at the Geological Survey of Israel (Wetzler et al., 2019). Data are extracted in 240 s windows starting 80 s before the event origin time, corrected for instrument response and the horizontal components are rotated to great circle path. Green's functions are computed using the frequency-wavenumber integration code (FKPROG) of Saikia (1994) based on the regional velocity model of Gitterman et al. (2002) with a 10 Hz sampling rate. For stations located within the DSB, we include a lowered velocity layer following Braeuer and Bauer (2015) representing the top sediments layer of the basin (Fig. S3). Green's functions are band-pass filtered in the frequency band of 0.06–0.1 Hz for earthquake with magnitude $3.0 \le M_W \le 4.0$ (Fig. S4), and 0.5–1.0 Hz for $M_W \le 2.9$ (Fig. S5) to capture the high frequency seismic energy content of smaller magnitude earthquakes at closer range. The best result is achieved through a grid-search on the depth and choosing the moment tensor solution and centroid depth for which the variance reduction (VR) is at maximum. Solutions are obtained with maximum number of seismic stations that results variance reduction above 50% and a minimum number of 3 stations. Depth is obtained from the maximum VR.

A total of 114 focal mechanisms are calculated for the basin (Fig. 2a) describing the entire ~35 time windows of our study (Fig. 4). About 46% of the focal-mechanisms indicate pure strike-slip faulting, and about same number of seismicity is recognized as oblique faulting (Fig. 2b).

Spatial examination of the focal mechanism distribution shows that the strike-slip faulting alternates between shallow (<12 km) at the EDSB (Fig. 5b) to relatively deep (≥12 km) faulting along the WDSB (Fig. 5c).

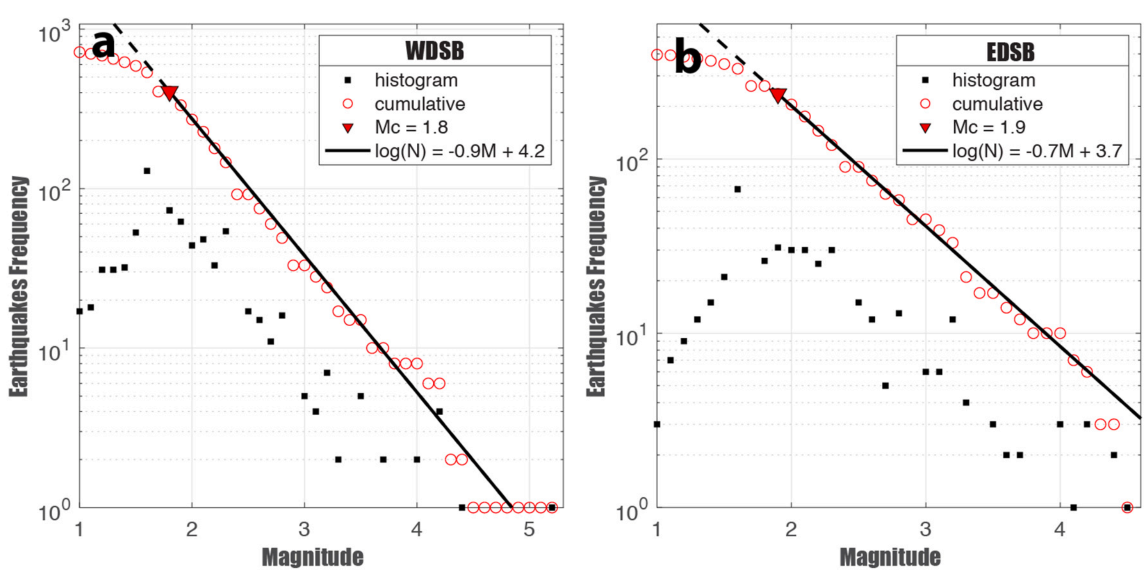

Fig. 3. Frequency-magnitude (Gutenberg-Richter) plots of the 1985–2021 seismicity divided to Western DSB (a), and Eastern DSB (b) (after Fig. 1b). Plotted: earthquake magnitudes frequency (black squares), cumulative magnitude frequency (red circles), and magnitude of data completeness (red triangle). (For interpretation of the references to colour in this figure legend, the reader is referred to the web version of this article.)

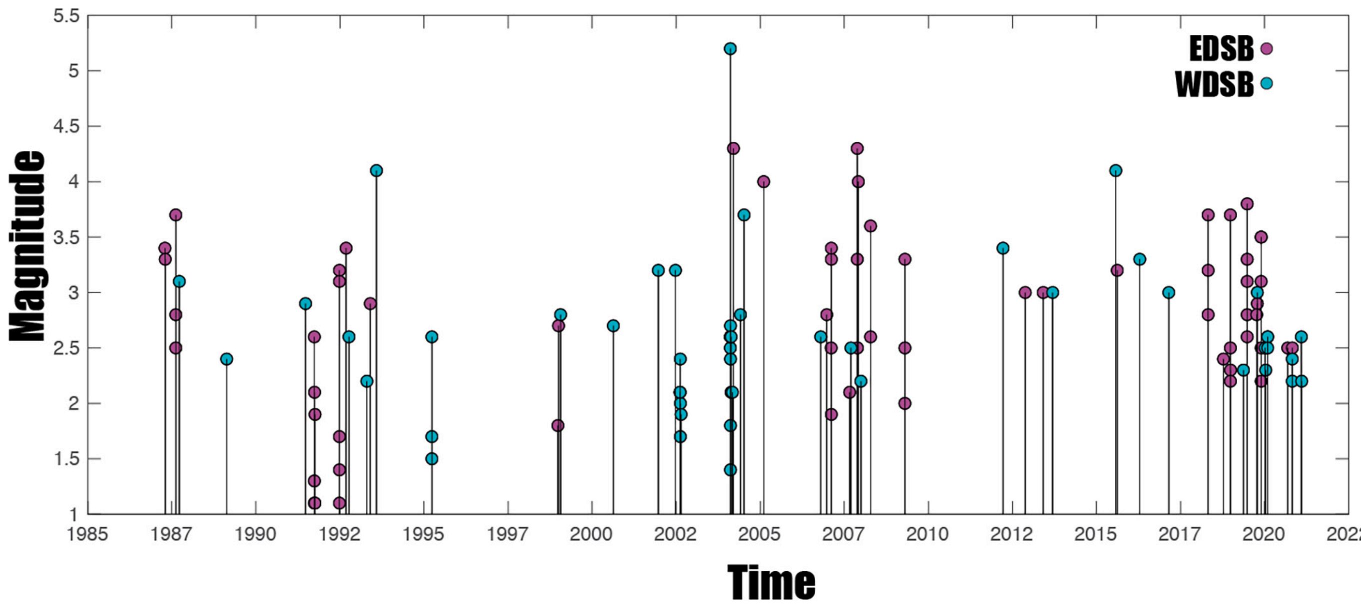

Fig. 4. Temporal occurrence of earthquakes in the two zones (legend) of the Dead Sea basin.

We also note a distinct pattern of normal faulting located at the central north section of the basin (Fig. 5c). Thus, our analysis clearly indicates asymmetry of the faulting style of small-earthquake along the basin.

2.3. Stress-inversion

To identify the fault plane from the two nodal planes, determine the faults frictional strength, and calculate the local stress field, we used stress-inversion approach developed to calculate the stress state associated with a set of focal mechanisms (Reches et al., 1992; Busetti and Reches, 2014). This approach was customized into MATLAB environment (https://github.com/nadavwetzler/Stress-Inversion) to calculate the orientations and relative magnitudes of the three principal stress axes (3D stress tensor) for a group of focal mechanisms under three assumptions: 1) All the earthquakes in the group occurred under the same stress state; 2) Slip along a fault occurs in the direction of maximum resolved shear stress, and 3) the shear and normal stress on the faults satisfy the Coulomb failure criterion. Each pair of the nodal planes is tested with respect to the *Principal Axes Misfit* angle (PAM), which is the angle between the ideal stress axes of each nodal plane and general stress axes of the entire group according to the optimal mechanical condition for faulting. The quality of the calculated stress tensor is represented by the confidence levels, calculated by bootstrapping method, for 500 random samples of the original focal mechanisms group. Stress is inverted for each friction coefficient, μ, that ranges between 0.1 and 0.8, weighted by the earthquake magnitude, and fault planes are selected according to smallest PAM between the two focal mechanisms nodal planes. To ensure coherent selection, two more criteria are set: 1) PAM is smaller than 30°, and 2) the aperture between the PAM of the two nodal planes is larger than 10%.

The inversion procedure begins with all possible planes of the focal mechanism dataset and with initial friction coefficient level of 0.1. After a general stress field is calculated, the PAM angles are calculated for each nodal plane and fault planes are selected according to the conditions described above, for a series of frictional coefficients. The optimal stress field is selected by the friction level that resulted maximum number of selected nodal planes under the conditions of a maximum angular misfit angle of ±25° following the uncertainty level of focal-mechanism data of the World Stress Map (Heidbach et al., 2010). The program calculates for each step the relative magnitudes of the principal stresses defined as $\phi = (\sigma_2 - \sigma_3) / (\sigma_1 - \sigma_3)$ (Angelier, 1984), and the stress ratio σ_1 / σ_2.

3. Stress field at the Dead Sea basin

3.1. Basin-wide stress state

We first analyze the stress state for the basin wide earthquake population. The initial solution of the inversion is calculated with $\mu = 0.1$ and yielded stress tensor of maximum (σ_1) and minimum (σ_3) principal stress axes at 319°/4° ± 10°, and 50°/5° ± 4°, respectively (Fig. S7a). The 114 focal mechanisms are tested with respect to the PAM angle, according to the conditions described above, resulting a total of 45 selected fault plane at $\mu = 0.1$ with sub horizontal principal axes: σ_1 at 317°/4° ± 8°, and σ_3 at 227°/2° ± 5° (Fig. 6a). We then increase the value of μ by 0.1 up to $\mu = 0.8$ and calculate the stress state for the selected fault planes for each individual friction coefficient. The number of selected fault planes increased to maximum of 69 planes at friction coefficient $\mu = 0.6$ (Fig. 6a). However, at this friction level of $\mu = 0.6$, the uncertainty of the maximum principal axis (σ_1) is large, ±49°. Therefore, we selected the solution obtained at $\mu = 0.3$ as the optimal friction coefficient for this group, including 58 planes (Fig. 6b). This basin-wide stress analysis demonstrates that the seismicity during the recent decades well represent the left-lateral faulting along the Dead Sea fault system and support the assumption that the chosen events occur under relatively homogeneous stress field. Below, we will refine this basin-wide stress-state.

3.2. Depth and spatial classification

To explore stress dependence on hypocenter depth, we divided the focal mechanism dataset into two groups based on depth distribution (Fig. 1b), with shallow group, depth < 12 km, of 29 earthquakes, and deep group, 12–30 km of 85 earthquakes (Fig. 7). The stress-inversion procedure was repeated for each group. The initial stress results, using all nodal planes in each group, are presented in Fig. S7b for the shallow and in Fig. S7c for the deep group.

Both focal mechanism groups present stable stress solutions throughout almost entire frictional range reconstructing the stress direction obtained at the previous stage (Fig. 6). For the shallow group, the maximum principal stress (σ_1) trend horizontally at ~326°, and the minimum principal stress (σ_3) trends horizontally at ~236° (Fig. 7a).

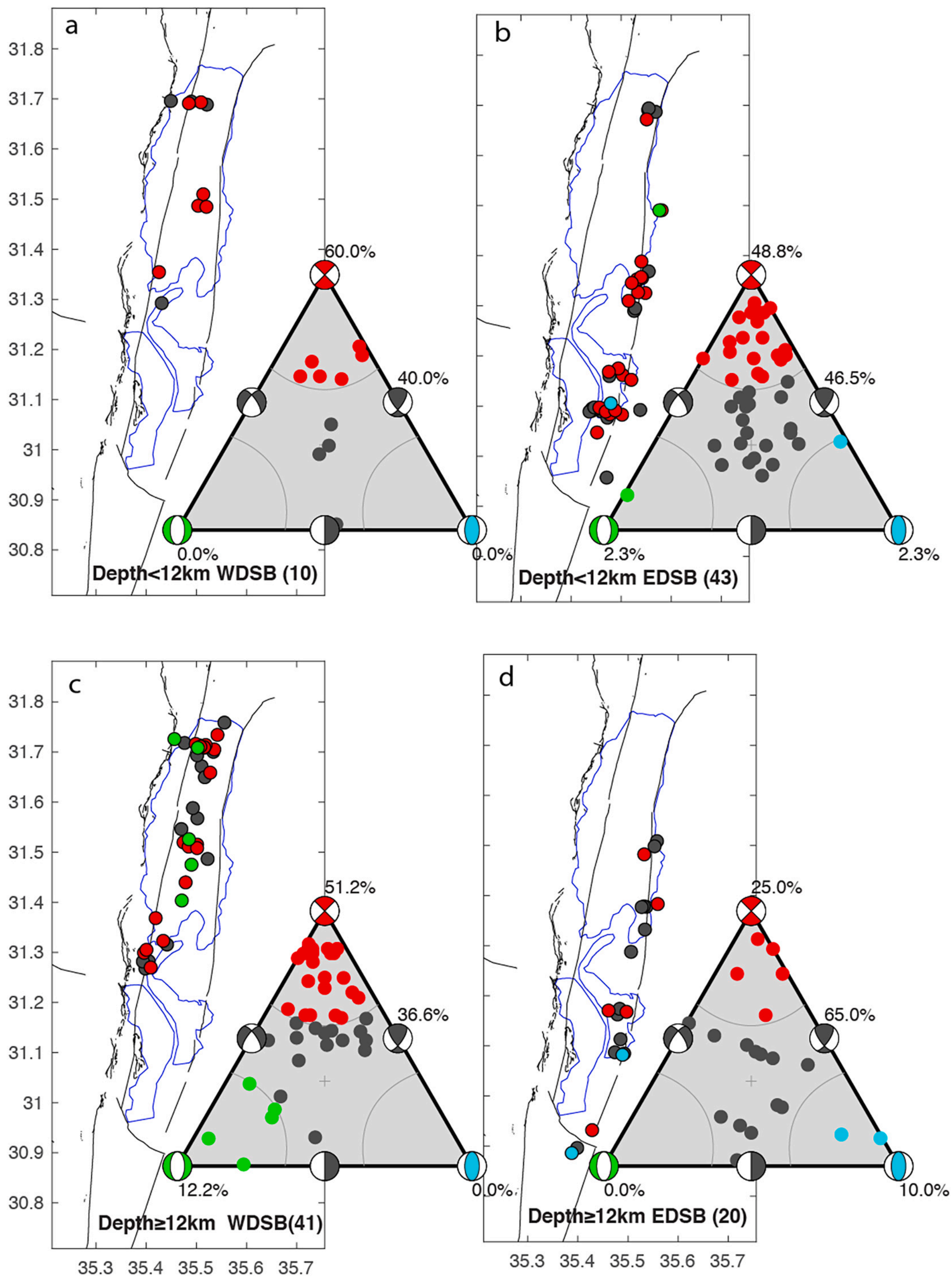

Fig. 5. Ternary plots of faulting styles based on focal mechanisms (symbols as in Fig. 2). Western DSB zone at <12 km depth (a), and at ≥12 km depth (c). Eastern DSB at <12 km depth (b), and at ≥12 km depth (d).

Maximum number of selected fault planes (17 out of 29 earthquakes) is obtained at $\mu = 0.3$ and remained constant up to $\mu = 0.8$ with a relatively low bootstrap uncertainty (<25°) up to $\mu = 0.7$. We select $\mu = 0.5$ as the optimal friction coefficient. The deep group constrained horizontal maximum and minimum principal axes with σ_1 trending at ~314°and σ_3 at 45° with the entire range of tested friction coefficients. Maximum number of selected fault planes (50) is obtained at $\mu = 0.5$ with bootstrap uncertainty of ±24° (Fig. 7b). We also note that the depth classification increased the total number of selected fault planes to 67, compared with the basin wide analysis (58 planes).

We continue with spatial classification of the focal mechanism dataset comparing the western and eastern fault zones of the basin (Fig. 1b). The Eastern DSB includes a total of 63 focal mechanisms, and the Western DSB 51 focal mechanisms. The Eastern DSB resulted a remarkably stable stress field, expressed by <20° bootstrap uncertainty of all stress axes, throughout the entire range of tested friction coefficients (Fig. 8a). Maximum number of selected fault planes (34) is obtained at $\mu = 0.5$ and remains constant up to $\mu = 0.8$. The maximum principal stress (σ_1) is constrained at ~143°, and minimum stress (σ_3) trends ~54° (Fig. 8a).

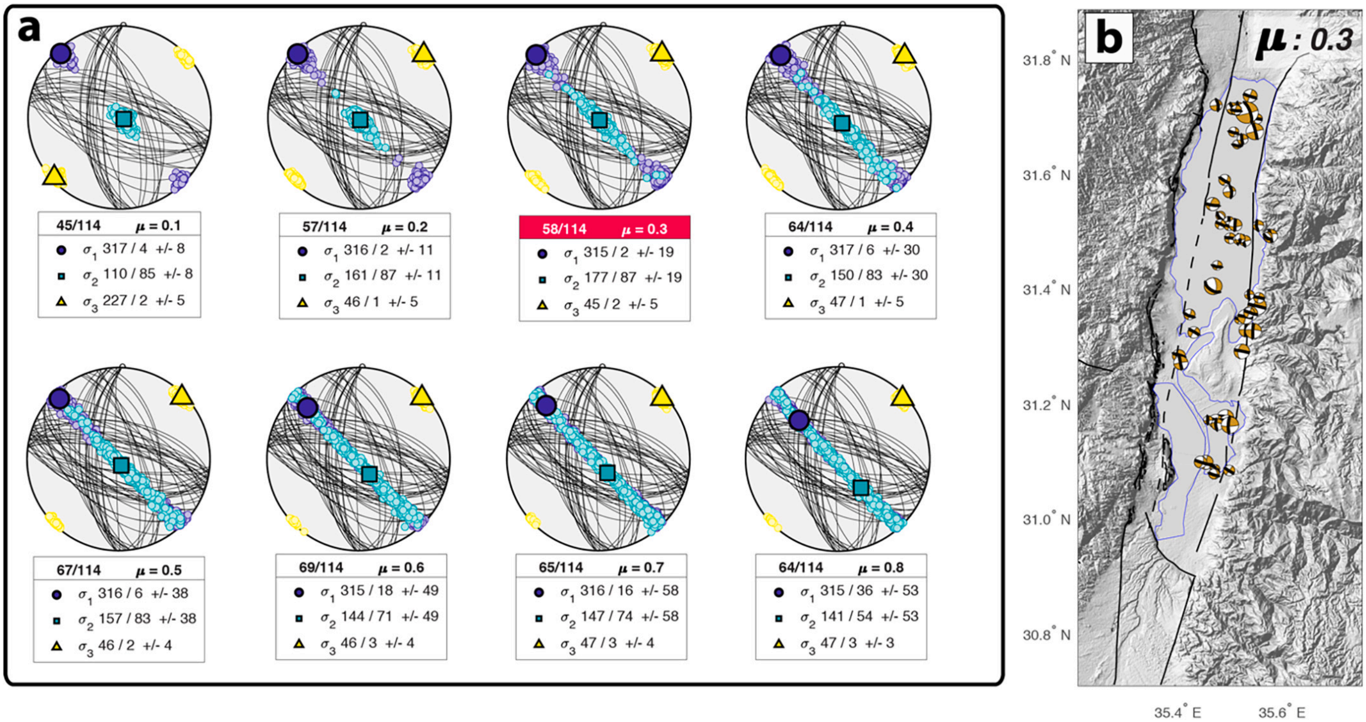

Fig. 6. (a) Stress-states in the Dead Sea basin calculated by stress-inversion of 114 focal mechanisms; lower hemisphere projection of principal stress axes with bootstrapping uncertainties, 500 re-samples for $\mu = 0.1$–0.8 (see text for details). The number of selected events for each friction coefficient solution is shown below each stereonet projection (e.g., 58/114 for $\mu = 0.3$). The orientations of the principal stress axes are noted in each solution with its standard deviation uncertainty. (b) The selected fault planes with friction coefficient $\mu = 0.3$, considered as the optimal friction coefficient with the maximum number of selected fault plains below bootstrap error angle of $\pm 25^{\circ}$ (see text). Selected planes are emphasized with solid black curve on each stereonet; also plotted are the main faults (black lines) and the 2021 lake coastline (blue lines). (For interpretation of the references to colour in this figure legend, the reader is referred to the web version of this article.)

The maximum number of selected fault planes (26) is obtained where $\mu = 0.3$ for the Western DSB and remained constant through the entire range of friction levels. The maximum principal stress (σ_1) is constrained between 312°–313°, and minimum stress (σ_3) trends 44° (Fig. 8b). We use $\mu = 0.5$ as the optimal coefficient for the two groups (Fig. 8b).

The number of selected fault planes has slightly increased (~10%) for the depth and spatial classification compared with the basin-wide group with similar calculated stress field for the selected datasets. We continue with geometrical examination of the resulted fault planes for the classified datasets.

3.3. Selection of fault planes

In general, the classified focal mechanisms groups (Fig. 7, Fig. 8) and the basin-wide stress fields (Fig. 6) can be directly associated with the far field paleo-stress field (Eyal and Reches, 1983). The calculated stress field is based on the planes selected by the criterions discussed in Section 2.3. The discrimination of the nodal planes depends on the PAM angles of the two nodal planes, which are systematically tested for a range of friction coefficients. During this process, about 50% of the focal mechanisms are selected with fault planes. From a mechanical point of view, we expect the larger magnitude earthquakes to reflect the regional stress field. Following this approximation, we find that the spatial classification better represents the larger magnitude range ($M \geq 4$) in the DSB (Fig. S6).

All the tested focal mechanisms groups yield similar orientations of the principal stresses. However, differences in the solutions are observed by the direction of the selected fault planes. The basin-wide group indicates that the fault planes trend at two distinct faulting direction: N-S and ENE – WSW, dipping from 45°-90° (Fig. 9a). These two fault orientations appear in different focal depths (Fig. 9b, c) and geographical zonation (Fig. 9d, e). The shallow, <12 km group and the Eastern DSB (Fig. 9d) are primarily (~65%) composed of N-S striking faults, mostly dipping between 60° and 80°. The deep >12 km group (Fig. 9c) and the Western DSB (Fig. 9e) include dominant ENE – WSW (~65%) and minor N-S faulting. Additional information is obtained from the rake angles of the selected fault planes (Fig. 8d). A comparison of the rake angles between the Western DSB and Eastern DSB shows that rakes at the Eastern DSB are confined to ~0° and ± ~180° associated with strike-slip faulting. Along the Western DSB, the rakes are distributed between −180° and 50°, indicating oblique normal and strike-slip faulting. This analysis is consistent with our previous observed asymmetry of the ongoing deformation along the basin (Figs. 1, 2, 5, 7, 8). The tectonic interpretation of these observations is discussed in Section 4.3.

4. Discussion

4.1. Application of stress inversion to seismological data

To incorporate the effect of fault frictional strength, we applied and enhanced the approach of Reches et al. (1992) for calculating regional stress and for selecting the fault planes. We develop a methodology for inverting for the principal stress axis based double couple focal mechanisms dataset at a range of friction coefficients. The process starts by initial calculation of the stress field at low friction coefficient; $\mu = 0.1$ (Fig. S7). In this case, the shear stresses along the two nodal planes are almost identical, and the inferred principal stress axes (σ_1 and σ_3) are closely oriented to the P and T axes (respectively) associated with the direction of the maximum, minimum seismic energy of the P wave radiation pattern. This strategy is implemented by previous stress-inversion codes such as SATSI algorithm (Hardebeck and Michael, 2006), which is widely utilized in many studies to calculate the stress field (e.g. Johnson et al., 2020; Martínez-Garzón et al., 2013; Yang and Hauksson, 2013).

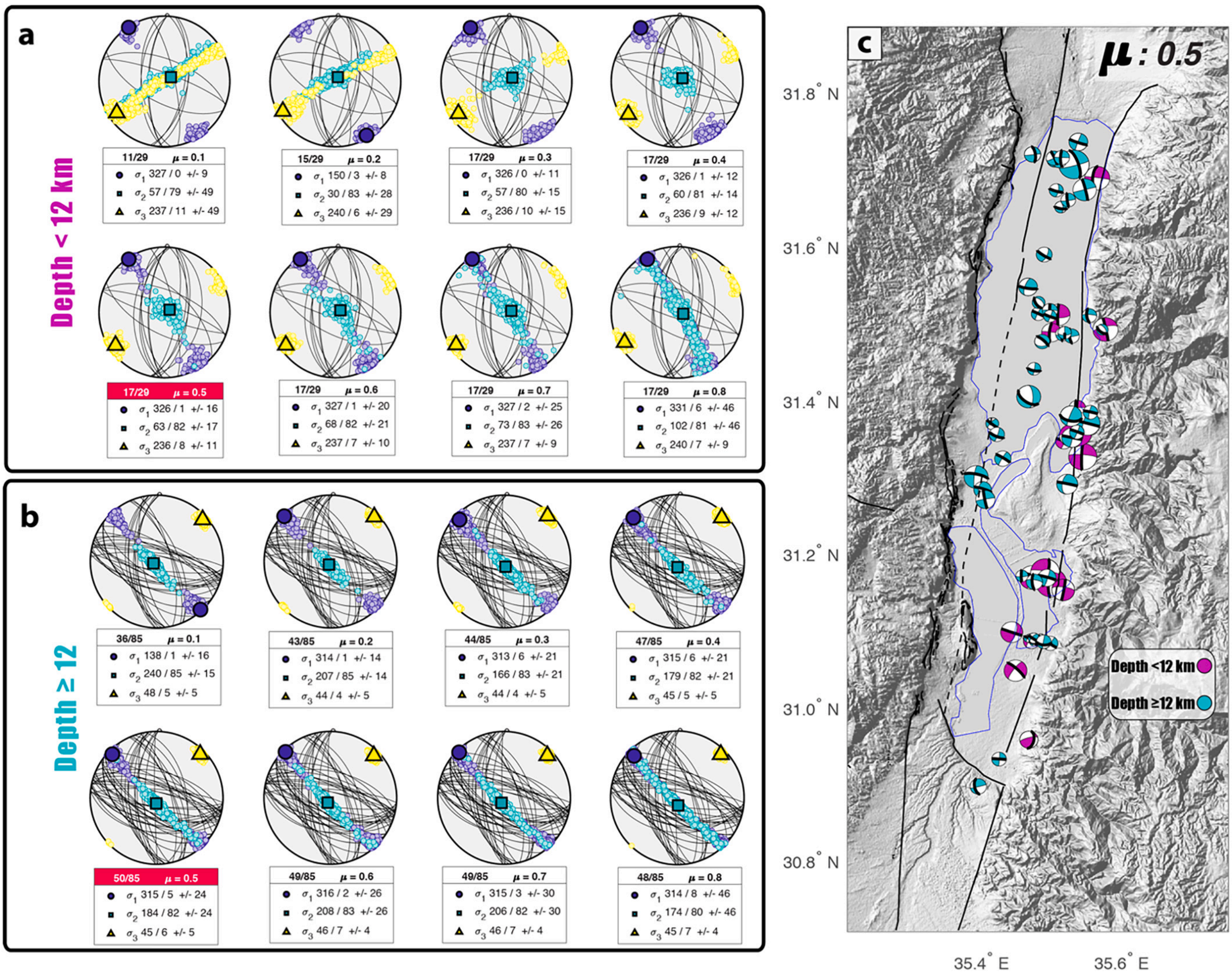

Fig. 7. The calculated stress-states in the DSB (Fig. 6) divided into two depth groups (Fig. 1b); (a) focal mechanisms of earthquake with depth < 12 km; (b) focal mechanisms of earthquakes of 12–30 km depth. (c) Plot of the focal mechanisms included in the stress calculation with $\mu = 0.5$ with selected planes marked by the solid thick black lines in each beachball diagram. Legend as in Fig. 6.

After the initial stress orientation is obtained, the two nodal planes are tested for a range of friction coefficients. At least for the case of the DSB, we find the inverted stress fields after selecting one fault planes (Figs. 6, 7, 8) are not distinctively different than the initial stress state obtained at low friction coefficient (Fig. S7). Alternatively, the process can start with higher friction levels, but doing that we find that the solution converges to a meaningless stress state represented by very few nodal planes. This is demonstrated in Fig. S8 for the basin-wide group with initial friction of $\mu = 0.5$.

The threshold of the PAM angle is selected empirically as 30° and was estimated from our multiple tests at a range of PAM thresholds (Table 1). In general, the number of selected nodal planes is dependent by the maximum PAM threshold. The tested end members 15° and 45° resulted in 26 and 88 selected nodal planes (respectively). Not surprisingly, the optimal friction coefficient was also found to be sensitive to the threshold of the PAM, indicating lower values of optimal friction coefficients with decreasing PAM threshold. The choice of 30° represents a conservative selection, based on the small contribution of higher value of PAM above 30° to the number of selected nodal planes.

4.2. The unselected events

While our stress inversion method and procedure calculate the stress tensor and assisted in the fault plane selection, it also filters out a relatively large number of focal mechanisms. For the condition we applied in our analysis, about 50% of the focal mechanisms are not associated with the regional stress field. We now focus on two examples of earthquakes clusters that deviates from the regional stress field.

Focal mechanisms of the 15-Aug-2002 to 20-Nov-2002 earthquake cluster in the northern part of the basin, including six events (events: 2266, 2269, 2270, 2276, 2271, 2281 and 2578, Table S1), show a repeating right-lateral strike-slip motion on a ~ N-S trending fault plane - opposite to the left-lateral motion along the Dead Sea transform or left-lateral motion on a E-W trending fault. This cluster was recognized by Wetzler et al. (2014) ~2 km south to the 2004 M5 cluster. Retrograde slip was also recognized after major earthquakes such as the 1989 Loma-Prieta earthquake (Aydin et al., 1992) and the 2019 Ridgecrest earthquake sequence (Xu et al., 2020). It was attributed to localized stress immediately after the main rupture. Therefore, it is difficult to explain the mechanical conditions for such behavior prior to the mainshock. Alternatively, dextral strike-slip on E-W trending faults is discussed by Christie-Blick and Biddle (1985) in the formation of 'Antithetic Shear' or

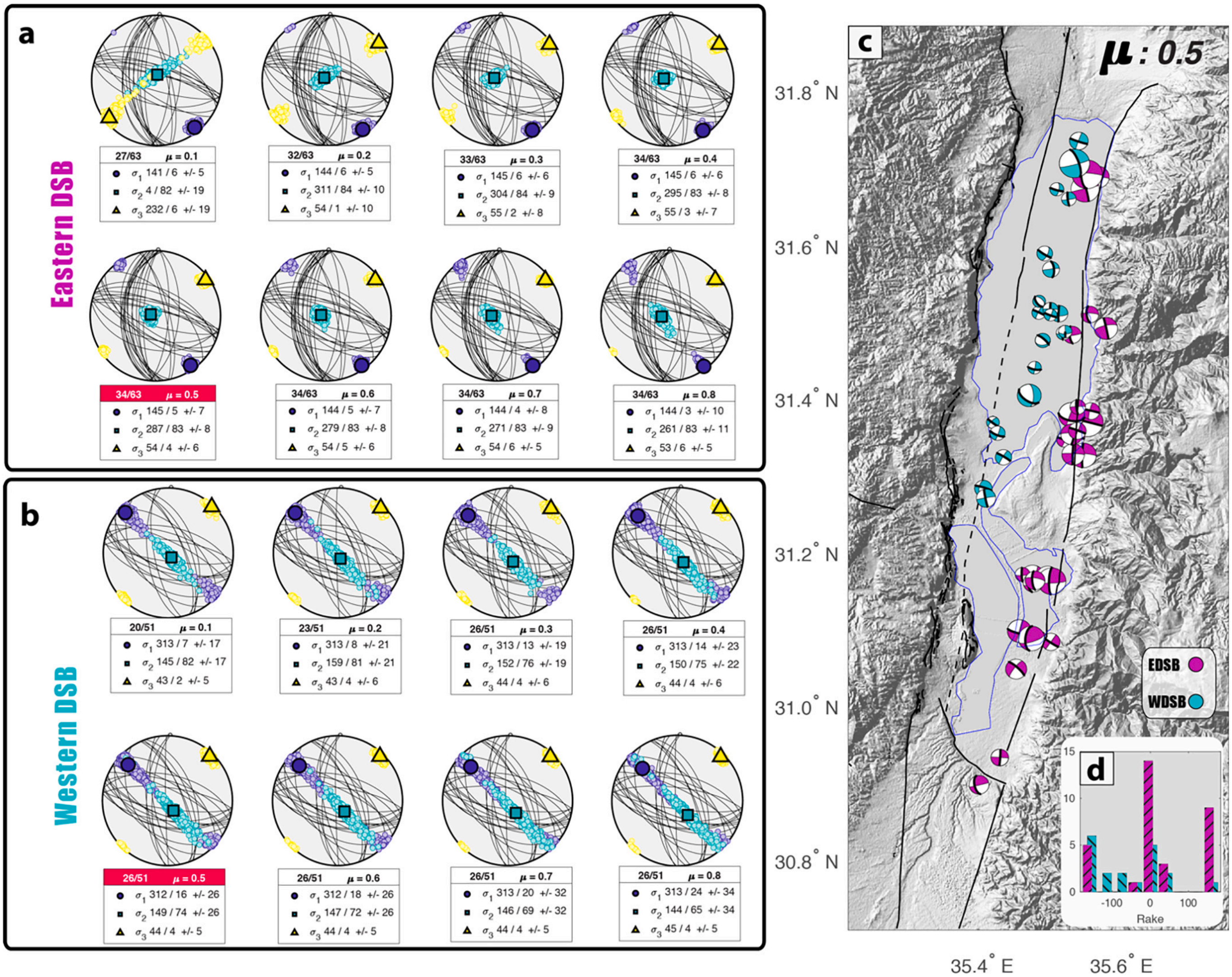

Fig. 8. The calculated stress-states in the DSB (Figs. 6, 7) divide into the Eastern zone (a) and Western zone (b); legend as in Fig. 6. (c) Focal mechanisms included in the stress field calculation using $\mu = 0.5$ and selected planes marked by the solid thick black lines on each beachball diagram. (d) Histograms of the rake angles of the fault planes selected by the stress-inversion method for friction coefficient $\mu = 0.5$ for the two zones.

a 'Conjugated Riedel Shear' scenarios. Other excluded planes include oblique (events: 2578, 2542, and 1166), reverse faulting (event 1625) and strike-slip (event 2615).

Another example is the aftershock sequence of the 2004 M5 earthquake (event 2237, Table S1) represented here by 12 focal mechanisms. Five aftershocks (events: 2345, 2380, 2382, 2409, 2436, Table S1) were excluded by the inversion method. Wetzler et al. (2014) suggested that the aftershocks of the 2004 M5 sequence were affected by local stress associated with the mainshock. Therefore, the stress inversion procedure not only important as a method for calculating stress and choosing the probable plane, but also for identifying local perturbations in the stress field.

4.3. Basin asymmetry and faulting style

Our examination of the seismicity at the Eastern and Western DSB, Fig. 1 shows clear spatial differences in the focal depth (Fig. 1), *b* value (Fig. 3), and faulting style (Fig. 5). The *b* value (Fig. 3) on the Western DSB is 0.7 whereas on the Eastern DSB it is 0.9. Typically, *b* values of 0.7 are associated with well-localized fault zone, as was shown for subduction zones (Schorlemmer et al., 2005). Low *b* value are also associated with relatively high deviatoric stresses (Scholz, 2015). Our stress inversion results are consistent with the relationship of high deviatoric stress and relatively low *b* value. The calculated differential stress (σ_1 - σ_3) of the shallow and Eastern DSB groups are systematically lower than the deep and Western DSB datasets (Fig. 10a, and b).

Comparison of faulting styles (Fig. 5) shows a clear partitioning of the strike-slip focal mechanisms between the shallow activity along the Eastern DSB (Fig. 5b) to deep along the Western DSB (Fig. 5c). In addition, we note a localized left-lateral strike-slip activity along the Eastern DSB, and mixed and oblique strike-slip and normal faulting along the Western DSB. This tendency of the deeper earthquakes to show oblique and normal slip components is compatible with the ratio between maximum principal stress (σ_1) and the intermediate principal (σ_2) stress (Fig. 10c, and d). We find a clear separation between the ratio σ_1/σ_2 at all tested friction coefficients between the two zones. The seismicity along the Western DSB indicates a σ_1/σ_2 ratio of ~1, demonstrating alternation of the maximum and intermediate principal stresses. We argue that the asymmetry observed between the two zones of the basin can be attributed to the fault configuration as observed by geological and geophysical studies, namely localized faulting along the eastern border and step-like faulting on the west (Garfunkel and Ben-Avraham, 1996). Our solutions suggest that more oblique faulting with sinistral and normal components occur in this zone. We further

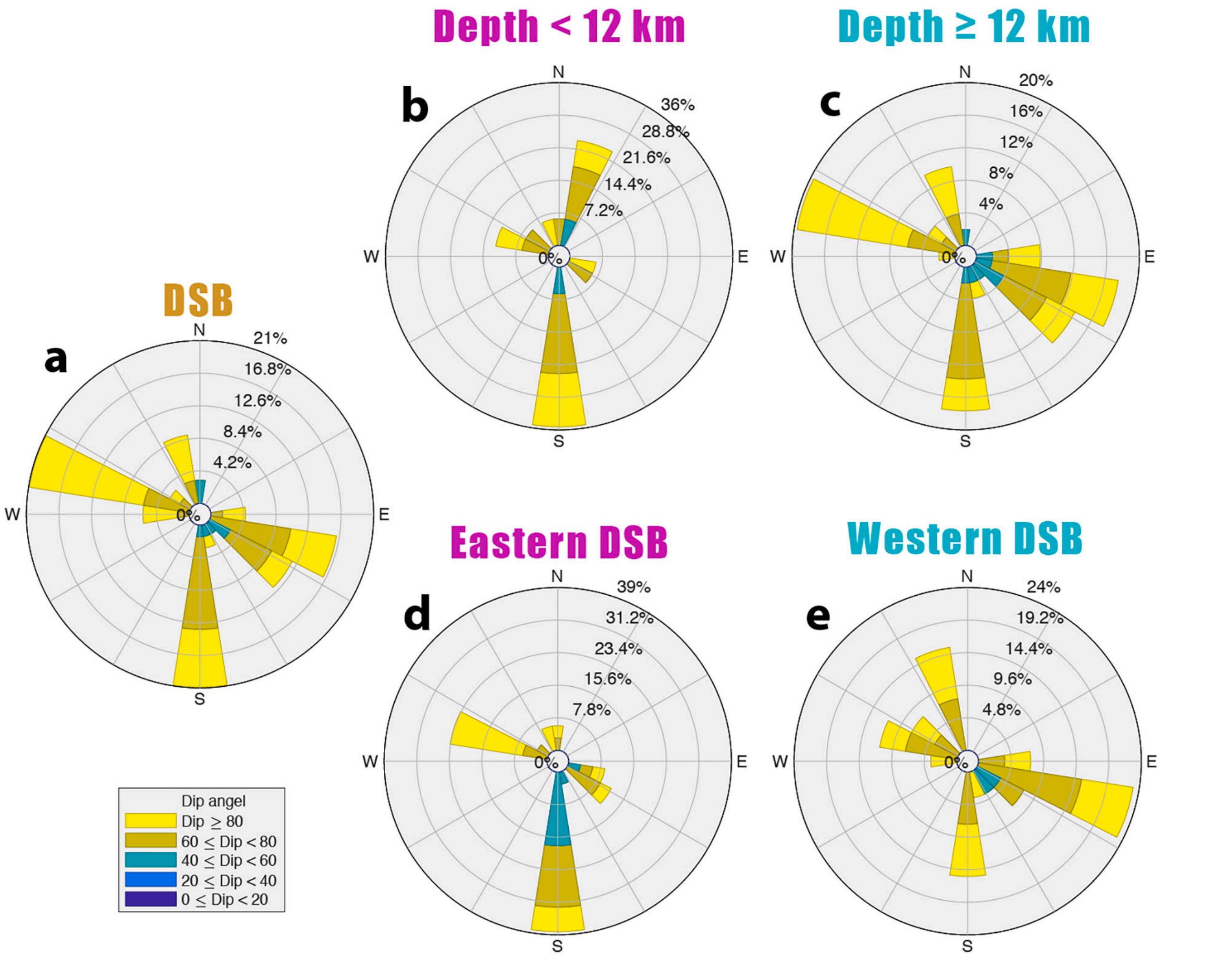

Fig. 9. Rose diagrams of the strike and dip of the fault planes selected by the stress-inversion method for friction coefficient $\mu = 0.5$ shown for five groups: basin-wide (a, Fig. 6b), depth groups (b, c, Fig. 7b), and spatial groups (d, e, Fig. 8b). The radii of the rose plots are marked by the shown percentages; MATLAB code for the rose diagrams by Pereira (2021). (For interpretation of the references to colour in this figure legend, the reader is referred to the web version of this article.)

Table 1
Number of selected planes at a range of Principal Axis Misfit (PAM) thresholds for the basin wide group. At each PAM threshold, the optimal friction coefficient (between 0.1 and 0.8) is selected by the maximum number of selected planes with maximum bootstrap angle of ±25°.

PAM threshold	Optimal μ	Selected plane	Bootstrap error
45	0.7	88	24
40	0.5	81	25
35	0.5	75	24
30	0.3	58	17
25	0.3	42	21
20	0.4	41	23
15	0.3	26	16

deduce that during the recorded period, the deformation along the eastern longitudinal fault was more localized than on the western zone; the later might consist of an ensemble of faults that accommodate both the strike-slip and the subsidence.

We also recognize deep normal faulting limited to the northern section of the basin. Deep seismicity between 25 and 29 km, which was recognized at the base of the crust (Braeuer et al., 2014, 2012), below the Lisan peninsula (Fig. 1b, Fig. S3), was associated with a decoupling zone (Mechie et al., 2009). Thermo-mechanical numerical evolutionary model of the DSB (Petrunin et al., 2012) suggests low frictional strength of the faults with friction coefficient of $\mu = 0.1$. The differences between the Eastern DSB and Western DSB described above, are not reflected by difference of frictional strength between the two spatial zones (Fig. 8) nor are the two depth groups (Fig. 7). The orientation of the stress principal axes of the DSB can be directly association with the large-scale paleo-stress field with an optimal friction coefficient of $\mu = 0.5$. The frictional properties of the crust generally agrees with previous studies (Reches et al., 1992; Shalev et al., 2013) indicating a cold and brittle crust up to the brittle-to-ductile transition at 30 km depth (Aldersons et al., 2003). However, it is possible that our dataset does not provide enough resolution to identify crustal weakening at depth.

5. Conclusions

By analyzing earthquake locations, faulting kinematics and stress field based on 114 small seismic events recorded within the DSB for 35 years, we identify a clear separation of the deformation style between the eastern and western longitudinal fault zones of the DSB. The spatial separation by 12 km depth (Fig. 1), followed by b value analysis is translated to differences of the focal mechanism and fault plane orientation. We suggest that the spatial differences in the seismicity express the basin structural asymmetry, which was noted by geological and geophysical studies. We find that ~50% of the focal mechanisms fit the long-term transform motion. The computed stress field fits the left lateral displacement along the Dead Sea transform, and the paleo-stress field determined by meso-structure kinematic markers (Eyal and Reches,

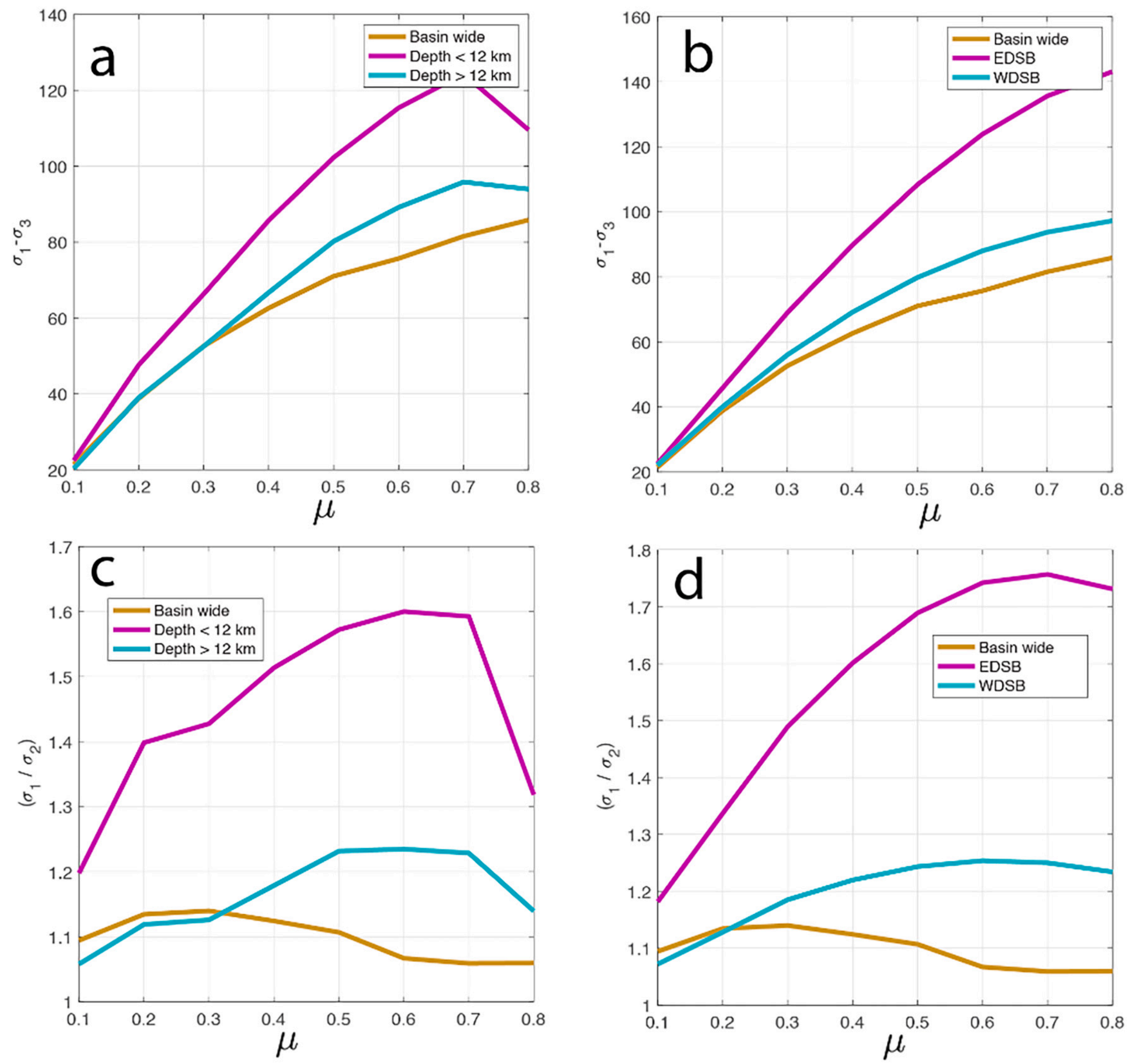

Fig. 10. The calculated differential stress (σ_1 - σ_3) (a, b), and the stress ratio σ_1/σ_2 (c, d) as function of the friction coefficient, μ (see text). The depth groups (a, c), and spatial groups (b, d) are marked in the legends.

1983). The best-fit friction coefficient for the DSB is $\mu = 0.5$, in agreement with Byerlee's law. We suggest that the strain partitioning between shallow strike-slip faulting and deep oblique-normal fault is a direct kinematic indication of the ongoing simultaneous subsidence and extension of the Dead Sea basin.

Declaration of Competing Interest

The authors declare that they have no known competing financial interests or personal relationships that could have appeared to influence the work reported in this paper.

Acknowledgements

We would like to thank Dr. Seth Busetti, Aramco Services, for providing the core MATLAB code for the stress-inversion. Thanks for two anonymous reviewers whose comments and suggestions significantly improved the manuscript. NW thanks the Israeli Science Foundation #363/20, and SM thanks the Israel Science Foundation grant #1645/19 for their financial support. We thank the analyst team of the Seismological Division of the Geophysical Institute of Israel for providing the seismological data.

Appendix A. Supplementary data

Supplementary data to this article can be found online at https://doi.org/10.1016/j.tecto.2021.229069.

References

Agnon, A., 2014. Dead Sea Transform Fault System: Reviews. https://doi.org/10.1007/978-94-017-8872-4.

Aldersons, F., Ben-Avraham, Z., Hofstetter, A., Kissling, E., Al-Yazjeen, T., 2003. Lower-crustal strength under the Dead Sea basin from local earthquake data and rheological modeling. Earth Planet. Sci. Lett. 214, 129–142. https://doi.org/10.1016/S0012-821X(03)00381-9.

Al-Zoubi, A., Shulman, H., Ben-Avraham, Z., 2002. Seismic reflection profiles across the southern Dead Sea basin. Tectonophysics 346, 61–69. https://doi.org/10.1016/S0040-1951(01)00228-1.

Angelier, J., 1984. Tectonic analysis of fault slip data sets. J. Geophys. Res. Solid Earth 89, 5835–5848. https://doi.org/10.1029/JB089iB07p05835.

Aydin, A., Nur, A., 1982. Evolution of pull-apart basins and their scale independence. Tectonics 1, 91–105. https://doi.org/10.1029/TC001i001p00091.

Aydin, A., Johnson, A.M., Fleming, R.W., 1992. Right-lateral-reverse surface rupture along the San Andreas and Sargent Faults associated with the October 17, 1989, Loma Prieta, California, earthquake. Geology 20, 1063–1067. https://doi.org/10.1130/0091-7613(1992)020<1063:RLRSRA>2.3.CO;2.

Ben-Avraham, Z., 1992. Development of asymmetric basins along continental transform faults. Tectonophysics 215, 209–220. https://doi.org/10.1016/0040-1951(92)90082-H.

Ben-Avraham, Z., ten-Brink, U.S., 1989. Transverse faults and segmentation of basins within the Dead Sea Rift. J. African Earth Sci. 8, 603–616. https://doi.org/10.1016/S0899-5362(89)80047-8.
Ben-Avraham, Z., Zoback, M.D., 1992. Transform-normal extension and asymmetric basins: an alternative to pull-apart models. Geology 20, 423–426. https://doi.org/10.1130/0091.
Braeuer, B., Bauer, K., 2015. A new interpretation of seismic tomography in the southern Dead Sea basin using neural network clustering techniques. Geophys. Res. Lett. 42, 9772–9780. https://doi.org/10.1002/2015GL066559.
Braeuer, B., Asch, G., Hofstetter, R., Haberland, C., Jaser, D., El-Kelani, R., Weber, M., 2012. Microseismicity distribution in the southern Dead Sea basin and its implications on the structure of the basin. Geophys. J. Int. 188, 873–878.
Braeuer, B., Asch, G., Hofstetter, R., Haberland, C., Jaser, D., El-Kelani, R., Weber, M.H., 2014. Detailed seismicity analysis revealing the dynamics of the southern Dead Sea area. J. Seismol. 18, 731–748. https://doi.org/10.1007/s10950-014-9441-4.
Brodsky, E.E., 2019. The importance of small earthquakes. Science (80-.) 79, 736–737.
Brothers, D.S., Driscoll, N.W., Kent, G.M., Harding, A.J., Babcock, J.M., Baskin, R.L., 2009. Tectonic evolution of the Salton Sea inferred from seismic reflection data. Nat. Geosci. 2, 581–584. https://doi.org/10.1038/ngeo590.
Busetti, S., Jiao, W., Reches, Z., 2014. Geomechanics of hydraulic fracturing microseismicity: Part 1. Shear, hybrid, and tensile events. Am. Assoc. Pet. Geol. Bull. 98, 2439–2457. https://doi.org/10.1306/05141413123.
Christie-Blick, N., Biddle, K.T., 1985. Deformation and Basin Formation along Strike-Slip Faults.
Dreger, D.S., Helmberger, D.V., 1993. Determination of source parameters at regional distances with three- component sparse network data. J. Geophys. Res. 98, 8107–8125. https://doi.org/10.1029/93JB00023.
Eyal, Y., Reches, Z., 1983. Tectonic analysis of the Dead Sea Rift Region since the Late-cretaceous based on mesostructures. Tectonics 2, 167–185. https://doi.org/10.1029/TC002i002p00167.
Freund, R., 1974. Kinematics of transform and transcurrent faults. Tectonophysics 21, 93–134. https://doi.org/10.1016/0040-1951(74)90064-X.
Frohlich, C., 2001. Display and quantitative assessment of distributions of earthquake focal mechanisms. Geophys. J. Int. 300–308 https://doi.org/10.1046/j.1365-246x.2001.00341.x.
Garfunkel, Z., 1981. Internal structure of the Dead Sea leaky transform (rift) in relation to plate kinematics. Tectonophysics 80, 81–108. https://doi.org/10.1016/0040-1951(81)90143–8.
Garfunkel, Z., Ben-Avraham, Z., 1996. The structure of the Dead Sea basin. Tectonophysics 266, 155–176. https://doi.org/10.1016/S0040-1951(96)00188-6.
Ginzburg, A., Ben-Avraham, Z., 1997. A seismic refraction study of the north basin of the Dead Sea, Israel. Geophys. Res. Lett. https://doi.org/10.1029/97GL01884.
Gitterman, Y., Pinsky, V., Shapira, A., Ergin, M., Kalafat, D., Gurbuz, G., Solomi, K., 2002. Improvement in detection, location, and identification of small events through joint data analysis by seismic stations in the Middle East/Eastern Mediterranean region 13 doi:DTRA01-00-C-0119.
Hardebeck, J.L., Michael, A.J., 2006. Damped regional-scale stress inversions: methodology and examples for southern California and the Coalinga aftershock sequence. J. Geophys. Res. Solid Earth 111, 1–11. https://doi.org/10.1029/2005JB004144.
Hardebeck, J.L., Shearer, P.M., 2002. A new method for determining first-motion focal mechanisms. Bull. Seismol. Soc. Am. 92, 2264–2276. https://doi.org/10.1785/0120010200.
Heidbach, O., Tingay, M., Barth, A., Reinecker, J., Kurfeß, D., Müller, B., 2010. Global crustal stress pattern based on the World Stress Map database release 2008. Tectonophysics 482, 3–15. https://doi.org/10.1016/j.tecto.2009.07.023.
Hofstetter, R., Klinger, Y., Amrat, A.-Q., Rivera, L., Dorbath, L., 2007. Stress tensor and focal mechanisms along the Dead Sea fault and related structural elements based on seismological data. Tectonophysics 429, 165–181. https://doi.org/10.1016/j.tecto.2006.03.010.
Hofstetter, R., Gitterman, Y., Pinksy, V., Kraeva, N., Feldman, L., 2008. Seismological observations of the northern Dead Sea basin earthquake on 11 February 2004 and its associated activity. Isr. J. Earth Sci. 57, 101–124. https://doi.org/10.1560/IJES.57.2.101.
Hofstetter, A., Dorbath, C., Dorbath, L., Braeuer, B., Weber, M., 2016. Stress tensor and focal mechanisms in the Dead Sea basin. J. Seismol. 20, 669–699. https://doi.org/10.1007/s10950-015-9550-8.
Imren, C., Le Pichon, X., Rangin, C., Demirbag, E., Ecevitoglu, B., Görür, N., 2001. The North Anatolian fault within the Sea of Marmara: a new evaluation based on multichannel seismic and multibeam data. Earth Planet. Sci. Lett. 186, 143–158. https://doi.org/10.1016/S0012-821X(01)00241-2.
Johnson, C.W., Fu, Y., Bürgmann, R., 2020. Hydrospheric modulation of stress and seismicity on shallow faults in southern Alaska. Earth Planet. Sci. Lett. 530, 115904. https://doi.org/10.1016/j.epsl.2019.115904.
Lockner, D.A., 1998. A generelized law for brittle deformation of Westerly granite. J. Geophys. Res. 103, 5107–5123.
Lubberts, R.K., Ben-Avraham, Z., 2002. Tectonic evolution of the Qumram Basin from high-resolution 3.5-kHz seismic profiles and its implication for the evolution of the northern Dead Sea Basin. Tectonophysics 346, 91–113. https://doi.org/10.1016/S0040-1951(01)00230-X.
Martínez-Garzón, P., Bohnhoff, M., Kwiatek, G., Dresen, G., 2013. Stress tensor changes related to fluid injection at the Geysers geothermal field, California. Geophys. Res. Lett. 40, 2596–2601. https://doi.org/10.1002/grl.50438.
Mechie, J., Abu-Ayyash, K., Ben-Avraham, Z., El-Kelani, R., Qabbani, I., Weber, M.H., 2009. Crustal structure of the southern Dead Sea basin derived from project DESIRE wide-angle seismic data. Geophys. J. Int. 178, 457–478. https://doi.org/10.1111/j.1365-246X.2009.04161.x.
Nof, R.N., Kurzon, I., 2020. TRUAA-earthquake early warning system for Israel: Implementation and current status. Seismol. Res. Lett. 92, 325–341. https://doi.org/10.1785/0220200176.
Palano, M., Imprescia, P., Gresta, S., 2013. Current stress and strain-rate fields across the Dead Sea Fault System: Constraints from seismological data and GPS observations. Earth Planet. Sci. Lett. 369–370, 305–316. https://doi.org/10.1016/j.epsl.2013.03.043.
Pereira, D., 2021. Wind Rose, MATLAB Central File Exchange. https://www.mathworks.com/matlabcentral/fileexchange/47248-wind-rose.
Petrunin, A.G., Meneses Rioseco, E., Sobolev, S.V., Weber, M.H., 2012. Thermomechanical model reconciles contradictory geophysical observations at the Dead Sea Basin. Geochem. Geophys. Geosyst. 13 https://doi.org/10.1029/2011gc003929.
Provost, A.-S., Houston, H., 2003. Stress orientations in northern and Central California: evidence for the evolution of frictional strength along the San Andreas plate boundary system. J. Geophys. Res. Solid Earth 108, 1–18. https://doi.org/10.1029/2001JB001123.
Reches, Z., 1987. Mechanical aspects of pull-apart basins and push-up swells with applications to the Dead Sea transform. Tectonophysics 141, 75–88. https://doi.org/10.1016/0040-1951(87)90175–2.
Reches, Z., Baer, G., Hatzor, Y., 1992. Constraints on the strength of the upper crust from stress inversion of fault slip data. J. Geophys. Res. 97, 12481. https://doi.org/10.1029/90JB02258.
Rivera, L., Cisternas, A., 1990. Stress tensor and fault plane solutions for a population of earthquakes. Bull. Seism. Sol. Am. 80, 600–614.
Sagy, A., Reches, Z., Agnon, A., 2003. Hierarchic three-dimensional structure and slip partitioning in the western Dead Sea pull-apart. Tectonics 22, 1–17. https://doi.org/10.1029/2001TC001323.
Saikia, C.K., 1994. Modified frequency-wavenumber algorithm for regional seismograms using Filon's quadrature: modelling of Lg waves in eastern North America. Geophys. J. Int. 118, 142–158. https://doi.org/10.1111/j.1365-246X.1994.tb04680.x.
Scholz, C.H., 2015. On the stress dependence of the earthquake b value. Geophys. Res. Lett. 42, 1399–1402. https://doi.org/10.1002/2014GL062863.
Schorlemmer, D., Wiemer, S., Wyss, M., 2005. Variations in earthquake-size distribution across different stress regimes. Nature 437, 539–542. https://doi.org/10.1038/nature04094.
Shalev, E., Lyakhovsky, V., Weinstein, Y., Ben-Avraham, Z., 2013. The thermal structure of Israel and the Dead Sea Fault. Tectonophysics 602, 69–77. https://doi.org/10.1016/j.tecto.2012.09.011.
Shamir, G., 2007. The active structure of the Dead Sea Depression. Spec. Pap. 401 New Front. Dead Sea Paleoenviron. Res. 2401, 15–32. https://doi.org/10.1130/2006.2401(02).
Shapira, A., Avni, R., Amos, N., 1993. A new estimate for the epicenter of the Jericho earthquake of 11 July 1927. Isr. J. Earth-Sci 42 (2), 93–96.
Sharon, M., Sagy, A., Kurzon, I., Marco, S., Rosensaft, M., 2020. Assessment of seismic sources and capable faults through hierarchic tectonic criteria: implications for seismic hazard in the Levant. Nat. Hazards Earth Syst. Sci. 20, 125–148. https://doi.org/10.5194/nhess-20-125-2020.
Sylvester, A.G., 1988. Strike-slip faults. Geol. Soc. Am. Bull. https://doi.org/10.1130/0016-7606(1988)100<1666.
ten-Brink, U.S., Flores, C.H.H., 2012. Geometry and subsidence history of the Dead Sea basin: a case for fluid-induced mid-crustal shear zone? J. Geophys. Res. Solid Earth 117, B01406. https://doi.org/10.1029/2011JB008711.
ten-Brink, U.S., Ben-Avraham, Z., Ben-Avraham, Z., 1989. The anatomy of a pull-apart basin: seismic reflection observations of the Dead Sea Basin. Tectonics 8, 333–350.
Vavryčuk, V., 2014. Iterative joint inversion for stress and fault orientations from focal mechanisms. Geophys. J. Int. 199, 69–77. https://doi.org/10.1093/gji/ggu224.
Wetzler, N., Sagy, A., Marco, S., 2014. The association of micro-earthquake clusters with mapped faults in the Dead Sea basin. J. Geophys. Res. Solid Earth 119, 8312–8330. https://doi.org/10.1002/2013JB010877.
Wetzler, N., Shalev, E., Göbel, T., Amelung, F., Kurzon, I., Lyakhovsky, V., Brodsky, E.E., 2019. Earthquake swarms triggered by groundwater extraction near the Dead Sea Fault. Geophys. Res. Lett. 46 https://doi.org/10.1029/2019GL083491, 2019GL083491.
Xu, X., Sandwell, D.T., Ward, L.A., Milliner, C.W.D., Smith-Konter, B.R., Fang, P., Bock, Y., 2020. Surface deformation associated with fractures near the 2019 Ridgecrest earthquake sequence. Science (80-.) 370, 605–608. https://doi.org/10.1126/science.abd1690.
Yang, W., Hauksson, E., 2013. The tectonic crustal stress field and style of faulting along the Pacific North America plate boundary in southern California. Geophys. J. Int. 194, 100–117. https://doi.org/10.1093/gji/ggt113.
Zak, I., Freund, R., 1981. Asymmetry and basin migration in the dead sea rift. Tectonophysics 80, 27–38. https://doi.org/10.1016/0040-1951(81)90140-2.
Zohar, M., Marco, S., 2012. Re-estimating the epicenter of the 1927 Jericho earthquake using spatial distribution of intensity data. J. Appl. Geophys. 82, 19–29. https://doi.org/10.1016/j.jappgeo.2012.03.004.
Zohar, M., Salamon, A., Rubin, R., 2017. Earthquake damage history in Israel and its close surrounding - evaluation of spatial and temporal patterns. Tectonophysics 696–697, 1–13. https://doi.org/10.1016/j.tecto.2016.12.015.